ADVANCED OPTICAL MATERIALS
www.advopticalmat.de

Giant Non-Resonant Infrared Second Order Nonlinearity in γ-$NaAsSe_2$

Jingyang He, Abishek K. Iyer, Michael J. Waters, Sumanta Sarkar, Rui Zu, James M. Rondinelli, Mercouri G. Kanatzidis, and Venkatraman Gopalan**

Infrared laser systems are vital for applications in spectroscopy, communications, and biomedical devices, where infrared nonlinear optical (NLO) crystals are required for broadband frequency down-conversion. Such crystals need to have high non-resonant NLO coefficients, a large bandgap, low absorption coefficient, and phase-matchability among other competing demands; for example, a larger bandgap leads to smaller NLO coefficients. Here, the successful growth of single crystals of γ-$NaAsSe_2$ that exhibit a giant second harmonic generation (SHG) susceptibility of d_{11} = 590 pm V^{-1} at 2 µm wavelength is reported; this is ~18 times larger than that of commercial $AgGaSe_2$ while retaining a similar bandgap of ~1.87 eV, making it an outstanding candidate for quasi-phase-matched devices utilizing d_{11}. In addition, γ-$NaAsSe_2$ is both Type I and Type II phase-matchable, and has a transparency range up to 16 µm wavelength. Thus, γ-$NaAsSe_2$ is a promising bulk NLO crystal for infrared laser applications.

1. Introduction

The past decade has seen considerable interest in new nonlinear optical (NLO) crystals for infrared laser applications.[1–7] NLO crystals can combine or split photons to generate new colors starting from a given laser line.[8,9] They are thus used to produce coherent laser radiation over a broad spectral range from the ultraviolet to 15–20 µm and beyond, which is of great importance in many technologies, such as in medical surgery,[10] environmental monitoring,[11] and imaging devices.[12] Though many NLO materials such as $KTiOPO_4$ (KTP),[13] β-BaB_2O_4,[14] and $LiNbO_3$[15] have been employed for generating light in the visible regime, they are not suitable for the infrared region because of their lower conversion efficiencies and infrared absorption past 4.5–5 µm wavelength. Although there are several new highly promising materials emerging from various research laboratories,[16–18] currently only a few infrared NLO materials are commercially available such as $AgGaS_2$,[19] $AgGaSe_2$,[20–22] and $ZnGeP_2$.[23] A central goal of the laser materials community is to develop new NLO crystals to complement and improve upon the current commercial crystals. This is by no means an easy task, since there are many competing demands on NLO crystals: high nonlinear coefficients, large transparency range, and hence, a large bandgap (which unfortunately scales inversely with nonlinear coefficients), low optical absorption coefficient, phase matchability of the NLO process for high efficiency conversion, the ability to grow large, high quality single crystals, and high laser damage threshold among others.[6,17,18,24]

Metal chalcogenides have attracted attention owing to their excellent optical properties arising from their more polarizable electron cloud and weaker interatomic bonds compared to oxides.[6,7] Among the promising infrared NLO materials, γ-$NaAsSe_2$ (**Figure 1**a; Figure S1, Supporting Information) exhibits several attractive properties. Its bandgap value of ~1.87 eV is comparable with that of $AgGaSe_2$ (1.80eV),[25] but the averaged SHG response is much greater than that of $AgGaSe_2$, characterized using the Kurtz–Perry powder technique.[26,27] Although this technique can quickly evaluate a potentially promising material, for practical applications, it is necessary to determine the complete anisotropic linear and nonlinear optical property tensors, which are accessible only in high-quality single crystals. The complete linear and nonlinear optical susceptibility tensors of γ-$NaAsSe_2$ have remained unknown since it was first grown in 2009, and only the bandgap and powder SHG were characterized.[27] Theoretical calculations on γ-$NaAsSe_2$ suggested a $\chi^{(2)}$ = 324.6 pm V^{-1} suggesting that this compound has the highest SHG response for materials with bandgaps greater than 1.5 eV.[28] One of the challenges in the synthesis of the γ-$NaAsSe_2$ is that it undergoes a phase transition very close to the melting point ~450 °C to the centrosymmetric δ-$NaAsSe_2$ upon reheating (Figure S2, Supporting Information). In this study, we have successfully

J. He, R. Zu, V. Gopalan
Department of Materials Science and Engineering
Pennsylvania State University
University Park, PA 16802, USA
E-mail: vxg8@psu.edu
A. K. Iyer, S. Sarkar, M. G. Kanatzidis
Department of Chemistry
Northwestern University
Evanston, IL 60208, USA
E-mail: m-kanatzidis@northwestern.edu
M. J. Waters, J. M. Rondinelli
Department of Materials Science and Engineering
Northwestern University
Evanston, IL 60208, USA
The ORCID identification number(s) for the author(s) of this article can be found under https://doi.org/10.1002/adom.202101729.

DOI: 10.1002/adom.202101729

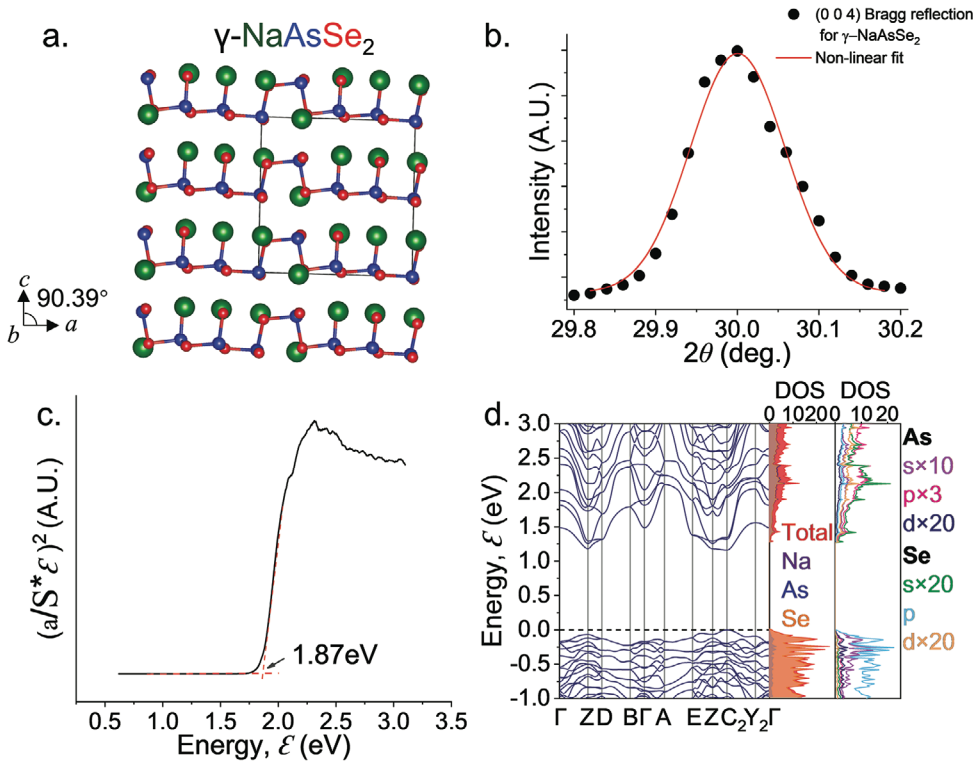

Figure 1. a) Crystal structure of γ-$NaAsSe_2$ viewed along the *b*-axis. b) (0 0 4) Bragg reflection peak fitted with a Gaussian function. c) Tauc plot of γ-$NaAsSe_2$ showing the direct bandgap of 1.87 eV. d) Band structure of γ-$NaAsSe_2$ with total DOS and PDOS of As and Se.

overcome this problem to grow large enough γ-$NaAsSe_2$ single crystals for the first time in order to fully characterize their anisotropic linear and NLO properties, something that was not possible earlier with crystals that were too tiny.[27] Single crystals of γ-$NaAsSe_2$ exhibit a giant second harmonic generation (SHG) susceptibility of d_{11} = 590 pm V^{-1} at 2 μm, as compared to 33 pm V^{-1} for $AgGaSe_2$ while retaining a similar bandgap of ~1.87 eV.[29] This makes it an outstanding candidate for exploring superior quasi-phase-matched devices. Using linear and nonlinear optical characterization combined with density functional theory, we determine that γ-$NaAsSe_2$ is both Type I and Type II phase-matchable. These outstanding properties suggest that γ-$NaAsSe_2$ could be a promising bulk NLO crystal for next-generation infrared laser applications.

2. Results and Discussion

γ-$NaAsSe_2$ crystallizes in the non-centrosymmetric monoclinic space group *Pc* and exhibits 1D infinite $[AsSe_2]^-$ chains connected via $AsSe_3$ units along the *a*-axis. For the first time, single crystals of γ-$NaAsSe_2$ were successfully grown using traditional solid-state reaction by melting the starting materials with sizes larger than 1mm^2 in dimensions, details of which can be found in the Experimental Section. Single crystal X-ray diffraction (XRD) was performed for structural determination and detailed crystallographic data and the atomic coordinates are shown in Tables S1 and S2, Supporting Information. Successful synthesis of the γ-$NaAsSe_2$ phase was also possible by the Bridgeman method at very slow translation speeds (0.5 mm h^{-1}), see the Supporting Information. Since the undesirable δ-$NaAsSe_2$ phase is only obtained upon remelting the γ-$NaAsSe_2$, single crystals of the γ-$NaAsSe_2$ phase were obtained either by the Bridgeman method or by the traditional solid-state reaction by melting the starting materials (cooling rate of 1.25 °C h^{-1}, see Experimental Section). The obtained ingot and crystals from both methods are shown in Figure S1, Supporting Information. γ-$NaAsSe_2$ phase purity was confirmed by using powder XRD data (Figure S3, Supporting Information). The cleaved single crystal obtained from the ingot was then studied by powder XRD by aligning the crystal in the direction of the x-ray without polishing. The full-width at half maximum (FWHM) of the (0 0 4) Bragg reflection was 0.13643 (6) degrees (Figure 1b). Attempts to grow larger high quality crystals for practical applications are currently underway.

Since the bandgap strongly limits both the laser damage threshold (LDT) and the SHG response of a material,[24,30] we characterized the optical transitions of γ-$NaAsSe_2$ using optical diffuse reflectance measurements converted to absorption data using the Kubelka–Munk equation.[31] The electronic band structure calculations on γ-$NaAsSe_2$ indicated a direct bandgap which is consistent with the optical absorption spectra which shows a value of 1.87 eV, as seen in Figure 1c. The spectra were derived by using the Kubelka–Munk function $(\alpha/S)^2$ versus energy for direct bandgap and $(\alpha/S)^{1/2}$ versus energy for the indirect bandgap (Figure S4, Supporting Information).[31–33] The upper wavelength limit of the transparency range of γ-$NaAsSe_2$ was determined by Fourier–transform infrared (FTIR)

spectroscopy . As shown in Figure S5, Supporting Information, the FTIR spectrum reveals that γ-$NaAsSe_2$ has no significant absorption up to at least 16 μm or 600 cm^{-1}, and therefore the wavelength transparency range of γ-$NaAsSe_2$ is 0.71 to at least 16 μm. Beyond 16 μm, the signal to noise ratio of the FTIR measurement did not allow us to determine the transparency. Theoretical prediction confirms the large transparency range as seen in Figure S6, Supporting Information.

To understand the electronic structure of γ-$NaAsSe_2$, we performed density functional theory (DFT) calculations using the PBE functional.[34] The electronic band structure of γ-$NaAsSe_2$ reveals relatively flat valence bands and a direct bandgap at the C_2 point of 1.18 eV, which is consistent with the well-known underestimation of band gaps by semi-local exchange-correlation functionals (Figure 1d). Atom-projected density of states (PDOS) indicate that the valence band comprises almost exclusively selenium *p* states with small contributions from arsenic *s* and *p* states near the valence band maximum which indicates partial ionicity. The mix of *s* and *p* arsenic states and the trigonal pyramidal coordination of the arsenic atoms with the three neighboring selenium atoms suggests that the covalency of the upper valence states is between the arsenic sp^3 orbitals and the selenium *p* states. Lower in the valence band, the arsenic contributes more proportionally to the total DOS.

We next investigated the linear optical properties of γ-$NaAsSe_2$. For a monoclinic system, there are three different coordinate systems that do not coincide with one another: crystallographic coordinates (*a, b, c*), crystal physics coordinates (Z_1, Z_2, Z_3), and principal eigen coordinates (Z_1^e, Z_2^e, Z_3^e). The crystallographic coordinates are defined as *a*//[100], *b*//[010], and *c*//[001]; The crystal physics coordinates are defined as Z_2//[010], Z_3//[001], and Z_1//$Z_2 \times Z_3$. In the principal Eigen coordinates, Z_2^e coincides with the *b* axis and the Z_2, the other two eigen axes are obtained by rotating the crystal physics axes about Z_2^e such that the dielectric tensor is diagonalized; α denotes the angle between Z_3 and Z_3^e, and it varies with wavelength. To study the linear optical properties of γ-$NaAsSe_2$, spectroscopic ellipsometry was used to obtain the complex refractive indices from 0.2 to 1 μm on three different orientations of the crystal. The ellipsometry spectra from all three sample orientations were fitted simultaneously to extract the complex refractive indices. DFT calculations were also performed to understand how the electronic structure produces the derived linear optical properties.

The measured and calculated refractive indices are shown in **Figure 2**. The anisotropic refractive index is defined as, $\tilde{n} = n + ik$. In the monoclinic system, the complex refractive indices have off-diagonal terms when expressed in the crystal physics coordinate. The dielectric tensor in this coordinate system (Z_1, Z_2, Z_3) is given by:

$$\tilde{\varepsilon} = \tilde{n}^2 = \begin{pmatrix} \tilde{n}_{11} & 0 & \tilde{n}_{13} \\ 0 & \tilde{n}_{11} & 0 \\ \tilde{n}_{13} & 0 & \tilde{n}_{33} \end{pmatrix}^2 \quad (1)$$

The *n* and *k* values shown in Figure 2 exhibit excellent qualitative agreement and a reasonable quantitative agreement that is typically considered acceptable in such comparisons, considering that DFT is not an excited state theory. For example, in both experiments and the DFT, we find a larger index in the [100] direction than in any other direction. We also find that the value of the off-diagonal element $\tilde{n}_{13}$ is very small and does not affect the fitting of other elements significantly. This can be attributed to the fact that the unit cell angle β is nearly 90°. In other words, the crystal physics axes and the principal eigen axes almost align with each other, and the crystal is practically optically orthorhombic. To confirm this hypothesis, the crystal was investigated with a polarizing microscope, similar to the method reported by Haertle et al.[35] The crystal was rotated about its [010] axis from the [001] axis until the measured intensity was minimal between a pair of cross polarizers. This angle, α, is the rotation angle between the crystal physics axis, Z_3 and the principal eigen axis, Z_3^e. From these measurements, it was found that $|\alpha| \leq 1.15°$.

Since the NLO properties of interest are at energies below the bandgap, the refractive indices from 0.7 to 1 μm were fitted to the Cauchy equation $n = A + \frac{B}{\lambda^2} + \frac{C}{\lambda^4} + \frac{D}{\lambda^6}$ and extrapolated to 2 μm, assuming the dispersion of *n* is small at lower energies. The parameters of the Cauchy equations are shown in

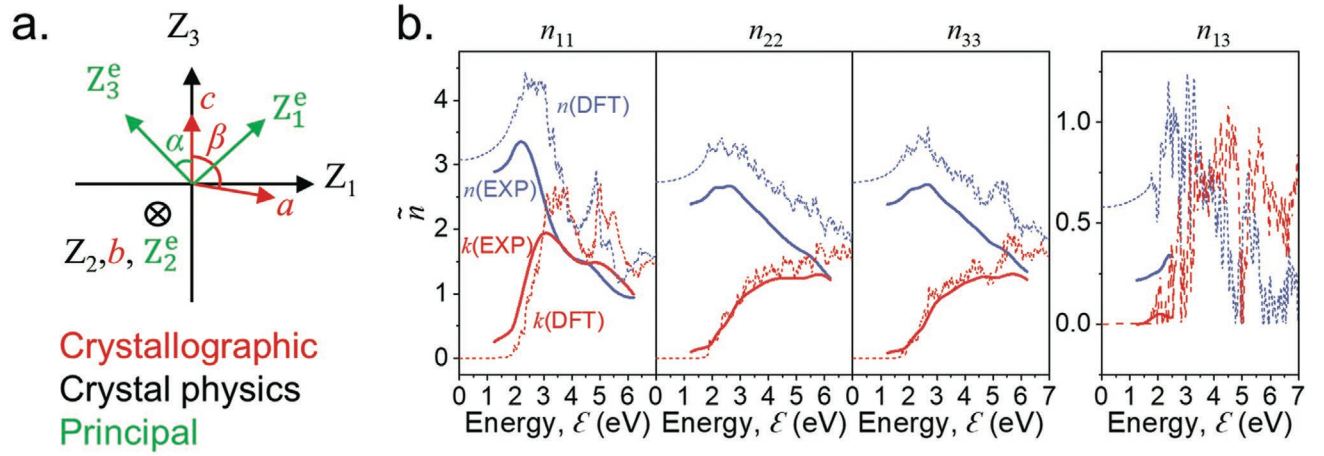

Figure 2. a) Three-coordinate systems for monoclinic materials. b) The experimental and calculated complex refractive indices of γ-$NaAsSe_2$ in the visible range. The blue and red curves are *n* and *k*, respectively.

Table 1. The parameters of Cauchy equations for the linear optical properties of γ-$NaAsSe_2$ in the crystal physics coordinate system, (Z_1, Z_2, Z_3), from 0.7 to 1 μm.

	A	B [μm²]	C [μm⁴]	D [μm⁶]
n_{11}	2.845	0.04496	−0.02974	0.03112
n_{22}	2.277	0.2022	−0.1249	0.03874
n_{33}	2.375	−0.004139	0.003537	0.01321
n_{13}	0.2122	0.001125	~0	0.003614

Table 1. These values were used for obtaining the second order NLO coefficients.

We next probe the second order nonlinear optical susceptibility of γ-$NaAsSe_2$. In the process of second harmonic generation (SHG), two photons of frequency ω combine to form one photon of frequency 2ω ($\omega + \omega = 2\omega$) through a nonlinear optical medium. The relationship between the nonlinear polarization and the electric field is $P_{i,2\omega} \propto d_{ijk}\, E_{j,\omega}\, E_{k,\omega}$, where d_{ijk} is the second-order optical susceptibility and E is the incoming electric field. The fundamental wavelength was chosen to be 2 μm such that the SHG wavelength was 1 μm, which is within the bandgap, and hence non-resonant and involving only virtual transitions; this minimizes the optical absorption loss. The second harmonic effect was then studied using SHG polarimetry as shown in **Figure 3**a.

The experiment was performed in normal reflection geometry, where the SHG intensities were measured as a function of polarization direction (ψ) of the incident field. The d tensor in crystal physics axes, (Z_1, Z_2, Z_3), for the point group m in Voigt notation is given as:

$$d = \begin{pmatrix} d_{11} & d_{12} & d_{13} & 0 & d_{15} & 0 \\ 0 & 0 & 0 & d_{24} & 0 & d_{26} \\ d_{31} & d_{32} & d_{33} & 0 & d_{35} & 0 \end{pmatrix} \quad (2)$$

The chosen sample geometry allows us to probe the d_{11} and d_{12} coefficients when the analyzer is set to be parallel to the Z_1 direction. Figure 3a depicts the measured polar plot fitted to an analytical model based on point group m:

$$I_{\parallel}^{2\omega} \propto \left|E_{\parallel}^{2\omega}\right|^2 \propto \left(d_{11} t_{\omega,\parallel}^2 \cos^2\psi + d_{12} t_{\omega,\perp}^2 \sin^2\psi\right) \quad (3)$$

where $t_{\omega,\parallel}$ and $t_{\omega,\perp}$ are the Fresnel transmission coefficients for the *p*-polarized and *s*-polarized light, respectively. The absolute magnitudes of the d coefficients can be obtained with respect to an *x*-cut $LiNbO_3$ whose backside is wedged and polished to eliminate the contribution from the back surface. The d_{33} of $LiNbO_3$ is ~ 18 pm V^{-1} at 2 μm using Miller's rule.[36,37] By comparing the SHG intensities of γ-$NaAsSe_2$ and $LiNbO_3$ at

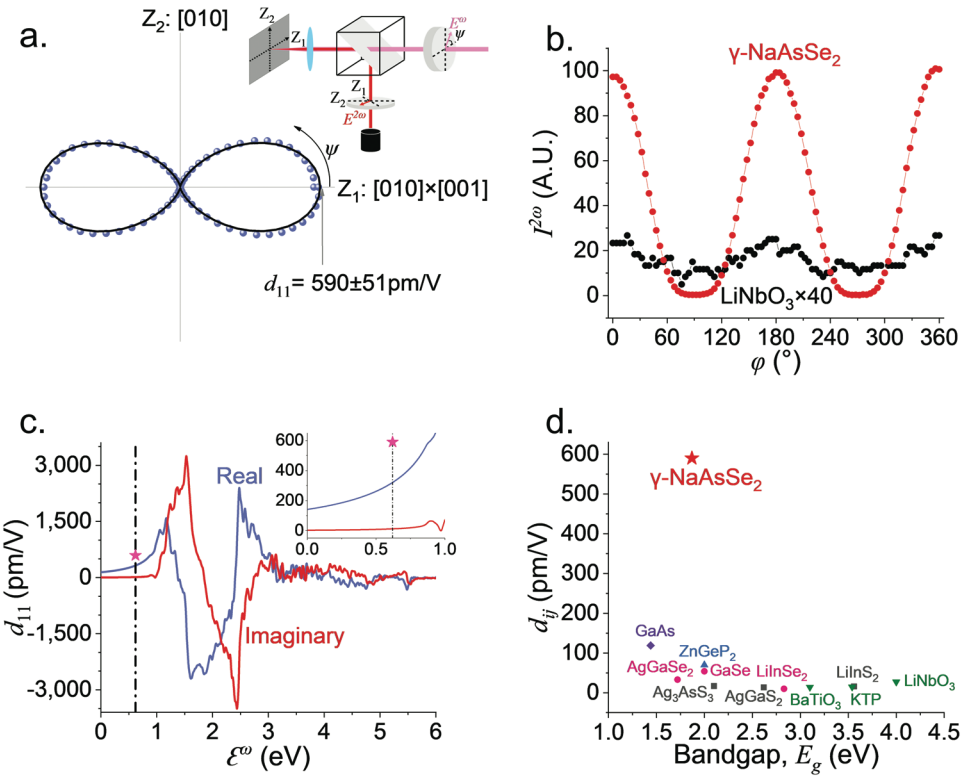

Figure 3. a) Polar plot of p-polarized SHG intensities generated from single crystal γ-$NaAsSe_2$. The black solid line is the simulated SHG values. The inset shows the experimental setup in normal reflection geometry. b) Comparison of the SHG intensities of γ-$NaAsSe_2$ and $LiNbO_3$, normalized to the same incident power. c) Calculated d_{11} versus energy. The pink star indicates the experimental value of d_{11}. The inset is an enlargement from 0 to 1 eV for clarity. d) Comparison of the highest SHG coefficient and bandgap of some well-known NLO crystals.

$\psi = 0°$ shown in Figure 3b, one can determine $d_{11} = 590 \pm 51$ pm V^{-1} using Equations (S1) and (S2), Supporting Information.[38,39] Figure 3c depicts the calculated complex d_{11} of γ-$NaAsSe_2$ as compared with the experimental value. The giant magnitude of d_{11} dominates both the polar plots and the ratio of d_{11}/d_{12}; therefore, even a small misalignment leads to the d_{11} "leaking into" the d_{12} value. Hence, only an upper limit for d_{12} can be determined. The ratio of d_{11}/d_{12} is found to be greater than 11, and hence $d_{12} <$ ~54 pm V^{-1}, an upper bound estimate. Additionally, SHG polarimetry was also performed at a wavelength of 3 µm with the same aforementioned experimental geometry to confirm the theoretical prediction of the small dispersion of d_{11} at energies below the bandgap. The d_{11} was extracted to be 577 ± 60 pm V^{-1} at 3 µm (Figure S7, Supporting Information). This confirms that the dispersion of d_{11} in the mid-infrared region is very small, and thus can be estimated to be ~570 pm V^{-1} in the 6–10 µm wavelength range using Miller's rule,[36] which suggests that γ-$NaAsSe_2$ has excellent NLO properties in the mid-infrared regime.

Figure 3d highlights the highest non-resonant SHG coefficient versus bandgap for some well-known NLO crystals. It clearly shows the general trend that crystals with larger bandgaps typically exhibit smaller SHG coefficients. However, d_{11} of γ-$NaAsSe_2$ exceeds the values in all the benchmark NLO crystals. It is worth noting that it surpasses the $d_{36} \approx 33$ pm V^{-1} of $AgGaSe_2$ by eighteen times, though its bandgap is comparable with that of $AgGaSe_2$.[40]

DFT calculations were performed to understand the origin of the larger linear and nonlinear optical response in the [100] direction than any other direction. From the imaginary components of the linear and nonlinear response spectra, the origin of these much larger responses is attributable to energies associated with low energy valence to conduction band excitations. The high DOS in the valence band and relatively flat bands from the selenium *p* states provide ample excitation routes, but this is true of all directions. The likely origin then is attributed to the arsenic–selenium chains extending along the [100] direction. Since lone electron pairs in the $[AsSe_2]^-$ chain are the likely origin of the strong SHG in the chain direction, and the flat bands indicate that the states are localized, we can construct a simple model combining the local hyperpolarizabilities into the net response.

For model simplicity, we will treat γ-$NaAsSe_2$ as ideal cubic. From the electron localization function (ELF) and chain orientation in **Figure 4**a,b, it can be seen that $[AsSe_2]^-$ chains comprise As atoms with one lone pair pointing in the <111> directions, the bridging Se atoms with two lone pairs pointing in the <110> directions, and Se^- anions with three lone pairs pointing in the <001> directions. The lone pairs of As, Se, and Se^- are treated as equivalent and multiple pairs lumped by projection onto a common axis as seen in Figure 4c. The contribution from each species are shown in **Table 2** and the individual atomic contributions are tabulated in Tables S4, S5, and S6, Supporting

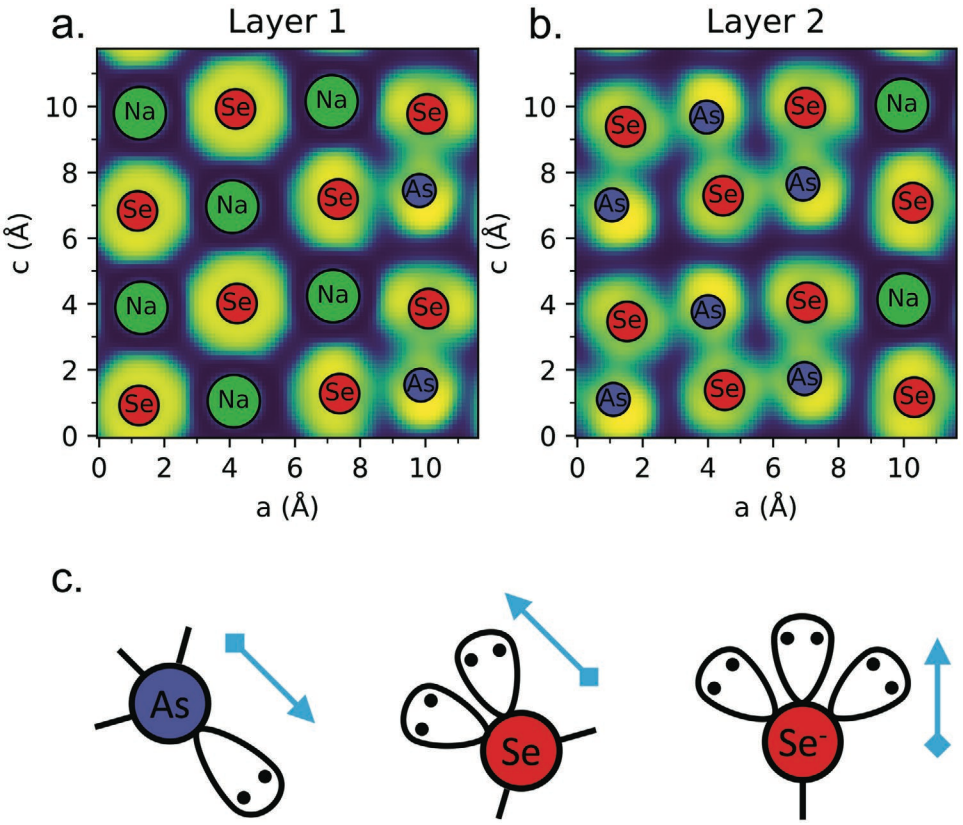

Figure 4. Plane slices of electron localization function computed at the mean b-axis position of each of the two atomic layers in the γ-$NaAsSe_2$ unit cell. a) The first layer has more Se^- anions with net lone pair vectors pointing perpendicular to the page. b) The second layer slices through more of the As and Se atom chains. c) A schematic showing the net lone pair vector orientations relative to the covalent bonds.

Table 2. The net lone pair vectors from each species and their sum. The nonlinear SHG coefficient is proportional to the square of the polarization vectors.[42]

Species	*a*-direction lone pairs	*b*-direction lone pairs	*c*-direction lone pairs
As	4.619	0	−2.309
Se	−6.532	0	0
Se^-	0	0	2.828
Sum	−1.913	0	0.519
Sum^2 $\propto d_{ij}$	3.660 $\propto d_{11}$	0 = d_{22}	0.270 $\propto d_{33}$

Information. This simple lone pair vector addition model predicts the strong d_{11}, zero d_{22}, and weak d_{33}, in agreement with the experiments. The d_{33}/d_{11} ratio predicted by the model is 7.4% which compares well to the static value of 5.1% calculated from the first-principles calculations. From the species breakdown in Table 2, it can be seen that the dominance of Se lone pairs over As lone pairs is the source high d_{11} and that the bridging Se atoms and the Se^- only have net contributions in the *a*- and *c*-directions respectively. These results underscore the importance of chain conformation on the SHG. For a more exact microscopic picture in future works, tools will need to be developed for spatial mapping of electron velocity matrix elements to permit direct inspection of important crystal features.[41]

It is interesting to compare the SHG conversion efficiency of γ-$NaAsSe_2$ to conventional NLO materials $LiNbO_3$, $AgGaSe_2$, and $ZnGeP_2$ at various wavelengths. The SHG intensity is proportional to d^2 and l^2, where d is the SHG coefficient and l is the distance that the light travels. When not phase-matched, the maximum SHG intensity is generated after traveling a distance of one coherence length, l_c.[43] The coherence length is defined as:

$$l_c = \frac{\lambda_\omega}{2(n_{2\omega} - n_\omega)} \tag{4}$$

in which $n_{2\omega}$ and n_ω are the refractive indices of the SHG and the fundamental beams. The coherence lengths for the largest SHG coefficients of γ-$NaAsSe_2$ and other NLO materials in the 1.5–2.5 µm spectral range are shown in **Figure 5**a. The coherence length of γ-$NaAsSe_2$ is much larger compared to other NLO materials and continues increasing in the infrared range. The promising coherence length will allow us to directly assess the d_{11} coefficient. The SHG conversion efficiency, normalized by I_ω^2 and l_c, can be calculated using the following equation:

$$\frac{I_{2\omega}}{I_\omega^2} = \frac{2\omega^2}{\varepsilon_0 c^3}\frac{d^2}{n_{2\omega}n_\omega^2}\frac{1}{l_c}\int_0^{l_c} l^2\,\mathrm{sinc}^2\left(\frac{\Delta k l}{2}\right)dl \tag{5}$$

where ε_0 is the vacuum permittivity and c is the speed of light, and Δk is the difference of the wave vectors of the SHG wave and fundamental wave. Figure 5b shows the non-phase-matched SHG conversion efficiency for the largest d coefficients of γ-$NaAsSe_2$ and the commercial NLO materials.[22] At 2 µm fundamental wavelength, non-phase-matched SHG from γ-$NaAsSe_2$ is nearly 300 times more efficient than $LiNbO_3$ and 500 times more efficient than $AgGaSe_2$. When compared with $ZnGeP_2$, the SHG conversion efficiency of γ-$NaAsSe_2$ is three orders of magnitude stronger. The chain-like characteristics which allow easy

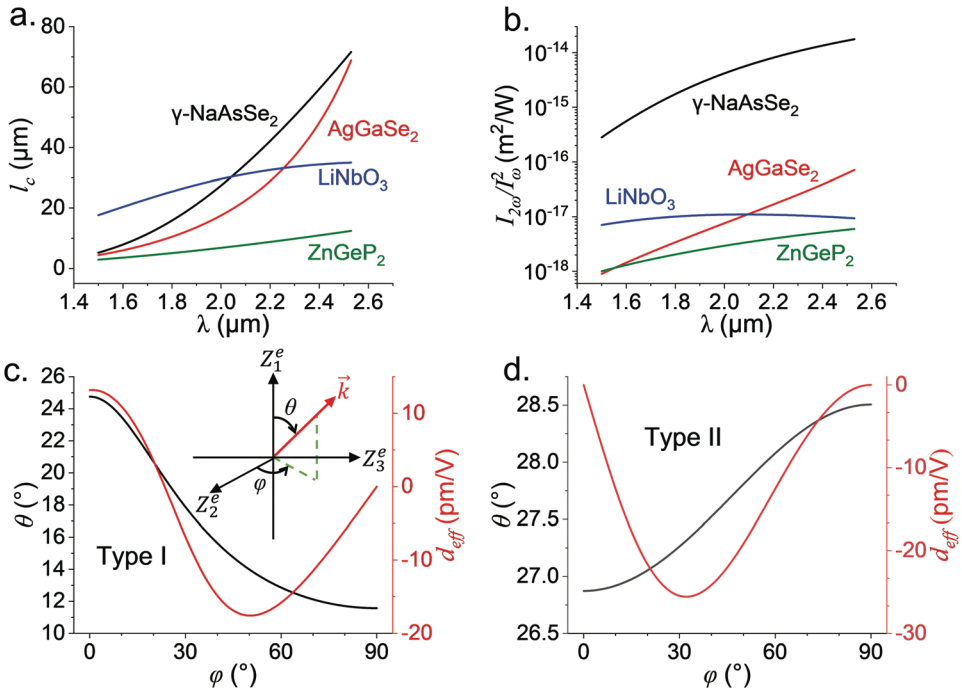

Figure 5. Comparison of a) coherence lengths and b) non-phase-matched SHG conversion efficiency between γ-$NaAsSe_2$ and conventional NLO materials. c) Type I and d) Type II phase matching angles (black) and d_{eff} (red) at 2 µm fundamental wavelength. Inset in (c) shows the definition of the phase matching angles θ and φ.

exfoliation, as well as solubility in strong polar solvents,[27] makes γ-$NaAsSe_2$ an excellent material for developing NLO thin films. The combination of both large d_{11} coefficient and coherence length makes this material an outstanding candidate for exploring orientation patterned quasi-phase-matching approaches.[44]

For applications which demand a high-power nonlinear conversion, the phase matching condition needs to be satisfied in order to eliminate restrictions on the crystal size used and to achieve the most efficient SHG.[45] Under this condition, Δk in Equation (5) equals 0; this implies that the refractive indices at ω and 2ω frequency should be equal. Figure 5c,d shows the Type I and Type II phase matching angles and the d_{eff} at 2 µm. The phase matching angles, θ and φ, are defined with respect to the Eigen direction, (Z_1^e, Z_2^e, Z_3^e) as shown in the inset of Figure 5c. Using the extrapolated refractive indices from Table 1 and the method reported by Yao and Fahlen,[46] we can then calculate θ and φ at 2 µm fundamental wavelength.[46] Based on the calculation, γ-$NaAsSe_2$ can be both Type I and Type II phase matched. The effective d coefficient, d_{eff}, can be estimated with the experimentally measured d_{11} and the other d coefficients from DFT (Figures S8 and S9, Supporting Information). At 2 µm fundamental wavelength, the maximum d_{eff} is –18 pm V^{-1} and –26 pm V^{-1} for Type I and Type II phase matching, respectively. These are comparable to the current commercial crystals of $d_{\text{eff}} \approx 13.4$ pm V^{-1} ($AgGaS_2$) and 26.8 pm V^{-1} ($AgGaSe_2$). The NLO crystals are typically professionally polished to optical grade and their surfaces are coated with anti-reflection coatings to prevent laser damage. Even without these steps, the laser-induced surface damage threshold (LISDT) of a cleaved γ-$NaAsSe_2$ surface (without polishing or coating) measured with ~27 ps pulses at 1.064 µm is comparable to that of commercially polished and coated $AgGaS_2$ crystals (see the Supporting Information).[47]

3. Conclusion

γ-$NaAsSe_2$ single crystals exhibit a giant second order nonlinearity with a remarkable optical SHG coefficient of d_{11} = 590 pm V^{-1} measured at 2 µm wavelength. This is the highest known non-resonant coefficient (see Figure 3d) for comparable optical bandgaps. For non-phase-matched SHG response generated in one coherence length, γ-$NaAsSe_2$ is two orders of magnitude more efficient than that of the conventional NLO materials at 2 µm fundamental wavelength, making it a highly promising candidate to explore toward orientation-patterned quasi-phase-matched devices.[44] In addition, it can also achieve both Type I and Type II phase matching with maximum $|d_{eff,I}| \approx 18$ pm V^{-1} and $|d_{eff,II}| \approx 26$ pm V^{-1} at 2 µm fundamental wavelength, which are comparable to the current commercial crystals of $AgGaS_2$ and $AgGaSe_2$. These promising optical properties make it a potential candidate to explore large crystals for bulk and quasi-phase-matched high infrared power generation in laser systems.

4. Experimental Section

Starting Materials: All manipulations were performed under dry nitrogen atmosphere in a glove box. Commercially available chemicals potassium sodium (Na, Sigma–Aldrich, 99.5%), arsenic (As, Alfa Aesar, 99.9%), and selenium (Se, American elements, 99.999%) were used without further purification. Na_2Se was prepared by modified literature procedure by reacting the alkali metals and selenium in liquid ammonia.[48] Warning: Elemental arsenic is highly toxic which must always be weighed out in the glovebox and precautions must be taken in preparing these samples.

Synthesis of the Title Compound γ-$NaAsSe_2$: Single crystals >2 mm of γ-$NaAsSe_2$ were grown by the combination of 0.732 g Na_2Se (5.85 mmol), 0.878 g As (11.72 mmol), and 1.388 g Se (17.57 mmol) which were thoroughly ground in the glovebox and loaded in a separate carbon coated fused-silica tube (13 mm OD). Carbon coated silica tubes were used to prevent tube attack from the alkali metal. The tube was then flame sealed under vacuum (≈3×10^{-3} mbar) and inserted in a single zone programmable vertical tube furnace. For the reaction in the vertical furnace, the temperature profile used was increasing to 500 °C in 12 h, annealed for 72 h and cooled to 350 °C over 120 h at which point the furnace was turned off. The phase purity of the sample was confirmed by using powder X-ray diffraction (XRD) particle size < 53 µm and comparing it with the simulated diffraction from the single crystal. Single XRD was performed on a crystal with dimensions $0.15 \times 0.14 \times 0.01$ mm^3 mounted on a glass fiber with epoxy for structure determination. A summary of the crystal data and refinement is provided in Table S1, Supporting Information. Final atomic coordinates and isotropic displacement (Uiso) are listed in Table S2, Supporting Information. To confirm the quality of the crystal obtained, the authors used powder XRD to obtain the diffraction on a cleave single crystal. The peak corresponding to the (0 0 4) Bragg reflection was then nonlinearly fitted to obtain the full-width at half maximum (FWHM).

Spectroscopic Ellipsometry: The spectroscopic ellipsometry was performed using a Woollam M-2000F focused beam spectroscopic ellipsometer on three different orientations of the crystal. The orientations are: 1. [001]// laboratory *z*, [010]// laboratory *x*; 2. [001] // laboratory *z*, [010] // laboratory *y*, and 3. [010]// laboratory *z*, [001]// laboratory *x*. The collected ellipsometric spectra were simultaneously fitted to Tauc–Lorentz oscillators and spline function for the diagonal terms and off-diagonal term, respectively. The parameters of the Tauc–Lorentz oscillators include an amplitude A_m, full width at half-maximum (FWHM) B_m, energy center $E_{0,m}$, and a Tauc gap $E_{g,m}$ (Table S3, Supporting Information).

SHG Measurements: The fundamental beam of 2 µm generated from a Spectra-Physics Ti: sapphire pumped OPA-800C (100fs, 1 kHz) was linearly polarized and rotated by an angle of ψ using a half waveplate and focused on the sample surface. The reflected second harmonic beam was filtered out by a dichroic mirror and detected by a photomultiplier tube after decomposition into a *p*-polarized and *s*-polarized light by an analyzer. An optical grade *x*-cut $LiNbO_3$ single crystal (MTI Corporation) was used as a reference.

DFT Calculations: All density functional theory (DFT) calculations were performed using the PBE functional.[34] ABINIT version 9.2.2 was used for linear and non-linear optical properties calculations.[49] Simulation preparation and post-processing were performed with the atomic simulation environment (ASE) version 3.19.1.[50]

Single point calculations were performed with ABINIT preceding the optical properties calculations within single particle approximation using the ABINIT utility, Optic. The Briliouin zone was sampled with a $4 \times 8 \times 4$ *k*-point grid. The plane wave cutoff was 1200 eV. The electronic solver convergence criterion was such that no energy eigen value changed by more than 10^{-6} eV between steps. Pseudopotentials from the standard accuracy, scalar relativistic set of the optimized norm-conserving Vanderbilt pseudopotentials (ONCV) version 0.4.0 were employed.[51] The number of empty bands was increased until the highest empty band was 20 eV above the valence band maximum which corresponds to 232 empty bands. Optics calculations within the independent particle approximation were performed using 50 meV broadening and with scissor shifts of 0.48 eV to compensate for the difference between the DFT fundamental gap and the experimentally measured bandgap.[52]

Supporting Information

Supporting Information is available from the Wiley Online Library or from the author.

Acknowledgements

J.H. and A.K.I. contributed equally to this work. J.H., A.K.I., S.S., M.G.K., and V.G. acknowledge the Air Force Office of Scientific Research Grant number FA9550-18-S-0003. M.J.W. and J.M.R. were supported by the National Science Foundation's (NSF) MRSEC program (DMR-1720139) at the Materials Research Center of Northwestern University. R.Z. and V.G. were supported by the NSF Materials Research Science and Engineering Center for Nanoscale Science, DMR-2011839. Scientific discussions and advice from Gary Cook, Carl M. Liebig, Ryan K. Feaver, Sean A. McDaniel, and Rita D. Peterson from the AFRL are gratefully acknowledged.

Conflict of Interest

The authors declare no conflict of interest.

Data Availability Statement

Research data are not shared.

Keywords

infrared nonlinear optical crystals, nonlinear optics, second harmonic generation

Received: September 18, 2021
Published online: November 9, 2021

[1] G. Dikic, B. Kovacevic, in *Satell. Cable Broadcast. Serv. TELSIKS 2001. Proc. Pap. (Cat. No.01EX517)*, **2001**, Vol. *2*, p. 745.
[2] B. Guo, Y. Wang, C. Peng, H. L. Zhang, G. P. Luo, H. Q. Le, C. Gmachl, D. L. Sivco, M. L. Peabody, A. Y. Cho, *Opt. Express* **2004**, *12*, 208.
[3] L. I. Isaenko, A. P. Yelisseyev, *Semicond. Sci. Technol.* **2016**, *31*, 123001.
[4] D. Pestov, X. Wang, G. O. Ariunbold, R. K. Murawski, V. A. Sautenkov, A. Dogariu, A. V. Sokolov, M. O. Scully, *Proc. Natl. Acad. Sci. USA* **2008**, *105*, 422.
[5] H. Zhou, L. Xiong, L. Chen, L. Wu, *Angew. Chem., Int. Ed.* **2019**, *58*, 9979.
[6] I. Chung, M. G. Kanatzidis, *Chem. Mater.* **2014**, *26*, 849.
[7] Q. Zhang, I. Chung, J. I. Jang, J. B. Ketterson, M. G. Kanatzidis, *Chem. Mater.* **2009**, *21*, 12.
[8] A. Marandi, N. C. Leindecker, V. Pervak, R. L. Byer, K. L. Vodopyanov, *Opt. Express* **2012**, *20*, 7255.
[9] R. W. Boyd, *Nonlinear Optics*, Academic Press, Cambridge, MA **2019**.
[10] V. A. Serebryakov, É. V. Boĭko, N. N. Petrishchev, A. V. Yan, *J. Opt. Technol.* **2010**, *77*, 6.
[11] M. Pushkarsky, A. Tsekoun, I. G. Dunayevskiy, R. Go, C. K. N. Patel, *Proc. Natl. Acad. Sci. USA* **2006**, *103*, 10846.
[12] *Mid-Infrared Coherent Sources and Applications* (Eds: M. Ebrahim-Zadeh, I. T. Sorokina), Springer, Berlin **2007**.
[13] J. D. Bierlein, H. Vanherzeele, *J. Opt. Soc. Am. B* **1989**, *6*, 622.
[14] C. Chen, B. Wu, A. Jiang, G. You, *Sci. Sin., Ser. B* **1985**, *28*, 235.
[15] G. D. Boyd, R. C. Miller, K. Nassau, W. L. Bond, A. Savage, *Appl. Phys. Lett.* **1964**, *5*, 234.
[16] F. Liang, L. Kang, Z. Lin, Y. Wu, *Cryst. Growth Des.* **2017**, *17*, 2254.
[17] X. Luo, Z. Li, Y. Guo, J. Yao, Y. Wu, *J. Solid State Chem.* **2019**, *270*, 674.
[18] A. Abudurusuli, J. Li, S. Pan, *Dalton Trans.* **2021**, *50*, 3155.
[19] M. C. Ohmer, R. Pandey, *MRS Bull.* **1998**, *23*, 16.
[20] P. G. Schunemann, K. L. Schepler, P. A. Budni, *MRS Bull.* **1998**, *23*, 45.
[21] G. C. Catella, D. Burlage, *MRS Bull.* **1998**, *23*, 28.
[22] D. N. Nikogosyan, *Nonlinear Optical Crystals: A Complete Survey*, Springer Science & Business Media, Berlin **2006**.
[23] P. D. Mason, L. F. Michaille, *Proc. SPIE* **2008**, *7115*, 71150N.
[24] A. G. Jackson, M. C. Ohmer, S. R. LeClair, *Infrared Phys. Technol.* **1997**, *38*, 233.
[25] A. Miller, G. S. Ash, *Opt. Commun.* **1980**, *33*, 297.
[26] S. K. Kurtz, T. T. Perry, *IEEE J. Quantum Electron.* **1968**, *4*, 333.
[27] T. K. Bera, J. I. Jang, J. H. Song, C. D. Malliakas, A. J. Freeman, J. B. Ketterson, M. G. Kanatzidis, *J. Am. Chem. Soc.* **2010**, *132*, 3484.
[28] J. H. Song, A. J. Freeman, T. K. Bera, I. Chung, M. G. Kanatzidis, *Phys. Rev. B: Condens. Matter Mater. Phys.* **2009**, *79*, 3.
[29] U. Simon, Z. Benko, M. W. Sigrist, R. F. Curl, F. K. Tittel, *Appl. Opt.* **1993**, *32*, 6650.
[30] X. Jiang, L. Kang, S. Luo, P. Gong, M.-H. Lee, Z. Lin, *Int. J. Mod. Phys. B* **2014**, *28*, 1430018.
[31] P. Kubelka, F. Munk, *Zh. Tekh. Fiz.* **1931**, *12*, 593.
[32] J. Tauc, R. Grigorovici, A. Vancu, *Phys. Status Solidi* **1966**, *15*, 627.
[33] *Optical Properties of Solids* (Ed: F. Abeles), Elsevier, Cambridge, MA **1972**.
[34] J. P. Perdew, K. Burke, M. Ernzerhof, *Phys. Rev. Lett.* **1996**, *77*, 3865.
[35] D. Haertle, A. Guarino, J. Hajfler, G. Montemezzani, P. Günter, *Opt. Express* **2005**, *13*, 2047.
[36] R. C. Miller, *Appl. Phys. Lett.* **1964**, *5*, 17.
[37] I. Shoji, T. Kondo, A. Kitamoto, M. Shirane, R. Ito, *J. Opt. Soc. Am. B* **1997**, *14*, 2268.
[38] W. N. Herman, L. M. Hayden, *J. Opt. Soc. Am. B* **1995**, *12*, 416.
[39] R. C. Haislmaier, N. J. Podraza, S. Denev, A. Melville, D. G. Schlom, V. Gopalan, *Appl. Phys. Lett.* **2013**, *103*, 031906.
[40] G. Boyd, H. Kasper, J. McFee, F. Storz, *IEEE J. Quantum Electron.* **1972**, *8*, 900.
[41] A. Taghizadeh, K. S. Thygesen, T. G. Pedersen, *ACS Nano* **2021**, *15*, 7155.
[42] T. Verbiest, K. Clays, C. Samyn, J. Wolff, D. Reinhoudt, A. Persoons, *J. Am. Chem. Soc.* **1994**, *116*, 9320.
[43] S. A. Denev, T. T. A. Lummen, E. Barnes, A. Kumar, V. Gopalan, *J. Am. Ceram. Soc.* **2011**, *94*, 2699.
[44] K. L. Vodopyanov, O. Levi, P. S. Kuo, T. J. Pinguet, J. S. Harris, M. M. Fejer, B. Gerard, L. Becouarn, E. Lallier, *Opt. Lett.* **2004**, *29*, 1912.
[45] W. Zhang, H. Yu, H. Wu, P. S. Halasyamani, *Chem. Mater.* **2017**, *29*, 2655.
[46] J. Q. Yao, T. S. Fahlen, *J. Appl. Phys.* **1984**, *55*, 65.
[47] H. J. Krause, W. Daum, *Appl. Phys. B: Photophys. Laser Chem.* **1993**, *56*, 8.
[48] T. J. McCarthy, M. G. Kanatzidis, *Chem. Mater.* **1993**, *5*, 1061.
[49] A. H. Romero, D. C. Allan, B. Amadon, G. Antonius, T. Applencourt, L. Baguet, J. Bieder, F. Bottin, J. Bouchet, E. Bousquet, F. Bruneval, G. Brunin, D. Caliste, M. Côté, J. Denier, C. Dreyer, P. Ghosez, M. Giantomassi, Y. Gillet, O. Gingras, D. R. Hamann, G. Hautier, F. Jollet, G. Jomard, A. Martin, H. P. C. Miranda, F. Naccarato, G. Petretto, N. A. Pike, V. Planes, et al., *J. Chem. Phys.* **2020**, *152*, 124102.
[50] A. H. Larsen, J. J. Mortensen, J. Blomqvist, I. E. Castelli, R. Christensen, M. Dułak, J. Friis, M. N. Groves, B. Hammer, C. Hargus, *J. Phys.: Condens. Matter* **2017**, *29*, 273002.
[51] D. R. Hamann, *Phys. Rev. B* **2013**, *88*, 85117.
[52] S. Sharma, C. Ambrosch-Draxl, *Phys. Scr.* **2004**, *T109*, 128.